Durham University

# Durham Research Online

## Deposited in DRO:

25 March 2020

## Version of attached file:

Published Version

## Peer-review status of attached file:

Peer-reviewed

## Citation for published item:

Mestre, Martín and Llinares, Claudio and Carpintero, Daniel D. (2020) 'Effects of chaos on the detectability of stellar streams.', Monthly notices of the Royal Astronomical Society., 492 (3). pp. 4398-4408.

## Further information on publisher's website:

https://doi.org/10.1093/mnras/stz3505

### Publisher's copyright statement:

This article has been accepted for publication in Monthly notices of the Royal Astronomical Society. ©: 2020 The Author(s) . Published by Oxford University Press on behalf of the Royal Astronomical Society. All rights reserved.

### Additional information:

### Use policy

The full-text may be used and/or reproduced, and given to third parties in any format or medium, without prior permission or charge, for personal research or study, educational, or not-for-profit purposes provided that:

- a full bibliographic reference is made to the original source
- a link is made to the metadata record in DRO
- the full-text is not changed in any way

The full-text must not be sold in any format or medium without the formal permission of the copyright holders.

Please consult the full DRO policy for further details.

Durham University Library, Stockton Road, Durham DH1 3LY, United Kingdom
Tel : +44 (0)191 334 3042 | Fax : +44 (0)191 334 2971
https://dro.dur.ac.uk

Monthly Notices
of the
ROYAL ASTRONOMICAL SOCIETY

MNRAS **492,** 4398–4408 (2020)
Advance Access publication 2019 December 13

doi:10.1093/mnras/stz3505

# Effects of chaos on the detectability of stellar streams

Martín Mestre,[1,2]★ Claudio Llinares[3,4] and Daniel D. Carpintero[1,2]

[1]*Instituto de Astrofísica de La Plata (CONICET-UNLP), B1900FWA, Argentina*
[2]*Facultad de Ciencias Astronómicas y Geofísicas de La Plata (UNLP), B1900FWA, Argentina*
[3]*Institute for Computational Cosmology, Department of Physics, Durham University, Durham DH1 3LE, UK*
[4]*Institute of Cosmology and Gravitation, University of Portsmouth, Dennis Sciama Building, Portsmouth PO1 3FX, UK*

Accepted 2019 December 9. Received 2019 November 13; in original form 2019 July 1

## ABSTRACT

Observations show that stellar streams originating in satellite dwarf galaxies are frequent in the Universe. While such events are predicted by theory, it is not clear how many of the streams that are generated are washed out afterwards to the point in which it is impossible to detect them. Here, we study how these diffusion times are affected by the fact that typical gravitational potentials of the host galaxies can sustain chaotic orbits. We do this by comparing the behaviour of simulated stellar streams that reside in chaotic or non-chaotic regions of the phase space. We find that chaos does reduce the time interval in which streams can be detected. By analysing detectability criteria in configuration and velocity space, we find that the impact of these results on the observations depends on the quality of both the data and the underlying stellar halo model. For all the stellar streams, we obtain a similar upper limit to the detectable mass.

**Key words:** chaos – Galaxy: kinematics and dynamics – galaxies: haloes.

## 1 INTRODUCTION

Observations show that the destruction of dwarf satellite galaxies due to tidal fields associated to the gravitational potential of the host galaxy is frequent (Mantha et al. 2018; Conselice, Yang & Bluck 2009; Kauffmann & White 1993). Stellar streams are unavoidable consequences, either permanent or transitory, of this type of interaction (Morales et al. 2018; Shipp et al. 2018; Martínez-Delgado et al. 2008). Although the main mechanism of stream formation and its relevance to the understanding of the origin and evolution of the Milky Way (MW) are well understood (e.g. Davies & Wright 1977; Wright 1972; Helmi et al. 1999; Helmi & White 1999), there is still much to be done on the application of stellar streams to galactic archaeology and cosmology. For instance, the properties of streams can be used to put constraints on the structure and evolution of the stellar and dark matter haloes of galaxies (Helmi et al. 2017; Malhan, Ibata & Martin 2018; Bovy 2016) as well as on the nature of the dark matter particles themselves (Banik et al. 2018). Regarding the intrinsic aspects of stellar streams, Amorisco (2015) made a theoretical and numerical characterization of three observable quantities: the speed of the stream's growth, the internal coherence of the stream, and its thickness or opening angle within and outside the orbital plane. Moreover, Hendel & Johnston (2015) and Karademir et al. (2019) have demonstrated that it is possible to relate orbital parameters of the orbits with their morphology: shell- or string-like shapes.

The study of stellar streams can be simplified by taking into account that the dynamics of the stars once they have been pulled out of the satellite depends almost exclusively on the properties of the gravitational potential of the host (i.e. self-gravity of the streams is negligible). Thus, we can apply tools and theorems that were built in the past for Hamiltonian systems with few degrees of freedom. Among them, chaos theory (Contopoulos 2002) is a well developed branch of study that has played a big role in many astrophysical theories, such as in Solar system dynamics (Morbidelli 2010; Tsiganis, Varvoglis & Dvorak 2005), multiplanet extrasolar systems (Martí, Giuppone & Beaugé 2013; Beaugé, Ferraz-Mello & Michtchenko 2012), barred spiral galaxies (Contopoulos & Harsoula 2012; Voglis, Tsoutsis & Efthymiopoulos 2006), and galaxy haloes (Zhu et al. 2017; Vallejo & Sanjuan 2016; Carpintero, Muzzio & Navone 2014; Efthymiopoulos, Voglis & Kalapotharakos 2007; Siopis & Kandrup 2000; Valluri & Merritt 1998; Merritt & Valluri 1996). And the field of stellar streams belongs to this group, since the early works of Hunter (2005), Fux (2001), and Dehnen (2000). Recently, Maffione et al. (2018, 2015) have shown that for stellar streams in the solar neighbourhood the effect of the chaotic mixing is negligible, in the sense that the proportion of erased substructure during a Hubble time is not significant. This is not in contradiction with the evidence about chaos affecting the morphology of streams whose progenitors are globular clusters (Bonaca et al. 2019; Price-Whelan et al. 2016a, b; Sesar et al. 2015; Fardal, Huang & Weinberg 2015; Pearson et al. 2015). This type of tidal streams are thinner and dynamically colder (Pearson et al. 2019; Lux et al. 2013) than those originated from dwarf satellite galaxies and the overall impact of chaos on streams born from these heavier progenitors is still uncertain.

★ E-mail: mmestre@fcaglp.unlp.edu.ar

© 2019 The Author(s)
Published by Oxford University Press on behalf of the Royal Astronomical Society

Downloaded from https://academic.oup.com/mnras/article-abstract/492/3/4398/5675643 by University of Durham user on 25 March 2020

Here, we study the relation between chaos and streams originated in dwarf-sized satellite galaxies embedded in the dark halo of a host galaxy similar to the MW. We do this by comparing the evolution of simulated streams that reside in chaotic and non-chaotic (regular) regions of the potential of the host. We measure the detectability of the streams by applying a simple criterion in either configuration or velocity space. We find that the presence of chaos does have an impact on the stream evolution. Streams that evolve in chaotic regions of the potential have shorter spans of detectability. We also find that the significance of this effect depends on details of the detectability criterion and the quality of the underlying stellar halo model.

A detailed description of the set up of the simulations is provided in Section 2. Our analysis techniques and definition of the detectability criterion that we applied to the data are presented in Section 3. The results of our work are given in Section 4. Finally, we discuss the results and conclude in Section 5.

## 2 SIMULATIONS

We study the impact that chaos has in the evolution of tidal streams by analysing simulated streams. The simulations consist in the *N*-body integrations of the trajectories of dark matter particles of a dwarf galaxy in a smooth gravitational potential that represents the MW. The integrations were made with the code GADGET-2 (Springel 2005). In order to work with a realistic satellite, we determine the initial conditions of its constituent particles to be consistent with a classical MW satellite (Wolf et al. 2010) such as Sculptor.

### 2.1 Host galaxy

The host galaxy is defined as a smooth analytic potential which we chose to be a generalized NFW potential (Navarro, Frenk & White 1997; Łokas & Mamon 2001):

$$\Phi(\boldsymbol{x}) = \Phi_{\rm NFW}(k(\boldsymbol{x})) = -\frac{GM_{200}}{f(c)}\frac{\ln(1+k(\boldsymbol{x})/r_{\rm s})}{k(\boldsymbol{x})}, \tag{1}$$

where $G$ is the gravitational constant, $M_{200}$ is the virial mass, $c$ is the concentration parameter, $r_{\rm s}$ is the virial radius ($r_{200}$) in units of the concentration, $k(\boldsymbol{x})$ parametrizes the asphericity of the halo, and the free function $f$ is given by $f(c) = \ln(1+c) - c(1+c)^{-1}$. We ussumed the following parameters: $G = 4.3009 \times 10^{-6}$ kpc km$^2$ s$^{-2}$, $M_{200} = 1.5 \times 10^{12}$ M$_\odot$ ($r_{200} = 242.40$ kpc), which are consistent with Dehnen, McLaughlin & Sachania (2006) and Watkins, Evans & An (2010) together with $c = 11.27$ in agreement with Burkert & Silk (1999) so that $r_{\rm s} = r_{200}/c = 21.51$ kpc.

The generalization of the spherical potential is given by a smooth transition between an axisymmetric potential in the inner region and a triaxial one in the outskirts, which is parametrized as follows

$$k(\boldsymbol{x}) = \left(\frac{1+r_{\rm t}(\boldsymbol{x})/r_{\rm g}}{1+r_{\rm a}(\boldsymbol{x})/r_{\rm g}}\right) r_{\rm a}(\boldsymbol{x}),$$

where we assumed a transition radius $r_{\rm g} = 1.2r_{\rm s} \approx 25.81$ kpc, as in Hayashi, Navarro & Springel (2007). The same parametrization was applied by Vera-Ciro & Helmi (2013) to a logarithmic potential (see also Vogelsberger et al. 2008). The function $r_{\rm a}$ that parametrizes the axisymmetric dependence was taken from Johnston, Law & Majewski (2005):

$$r_{\rm a} = \sqrt{x^2 + y^2 + (z/q_z)^2},$$

where $q_z = 0.93$ is consistent with fits to M-giants selected from the Two Micron All Sky Survey that correspond to tidal debris in the MW, performed by the same authors.

The other free function $r_{\rm t}$ provides the triaxial dependence and was taken from Law & Majewski (2010):

$$r_{\rm t} = \sqrt{C_1x^2 + C_2y^2 + C_3xy + (z/q_3)^2}, \tag{2}$$

were

$$C_1 = \frac{\cos^2\alpha}{q_1^2} + \frac{\sin^2\alpha}{q_2^2},$$
$$C_2 = \frac{\cos^2\alpha}{q_2^2} + \frac{\sin^2\alpha}{q_1^2},$$
$$C_3 = 2\cos\alpha\sin\alpha\left(\frac{1}{q_1^2} - \frac{1}{q_2^2}\right).$$

For the free parameters in these expressions, we chose values that were obtained by the same authors as best-fitting parameters to data of the Sagittarius dwarf galaxy: $\alpha = 97^\circ$, $q_1 = 1.38$, $q_2 = 1$, and $q_3 = 1.36$. Although Deg & Widrow (2013) found a model with similar shape and extreme orientation relative to the galactic disc, it is unstable according to Debattista et al. (2013) and thus improbable in standard cosmological simulations. The works of Pearson et al. (2015), Deg & Widrow (2014) and Vera-Ciro & Helmi (2013) provide further details about the unrealistic character of this model (i.e. the Law & Majewski 2010 triaxial potential with constant axial ratios). In spite of this, our aspherical MW halo model given in equation (1) is an example of a non-integrable gravitational potential whose phase space is inhabited by regular and chaotic orbits, thus serving for the purpose of this research.

### 2.2 Orbits of the progenitors

We integrated 12 satellites whose centre of mass have initial conditions given in either chaotic or regular regions of the phase space of the smooth host potential. Since the accessible regions of the phase space are too extensive to make a comprehensive dynamical study (i.e. they are 6D and unbounded), we decided to focus on the typical orbits that give birth to minor mergers. This is done by imposing a condition on the initial circularity $\eta$ of the orbits.[1] So, for all the orbits we fixed $\eta = 0.54$ which is the most probable value obtained in the cosmological simulations of Wetzel (2011). As we are interested in probing different galactocentric scales, we launch the orbits from apocentres at three typical distances: 30, 50, and 80 kpc. Working with spherical coordinates $r$ (radius), $\theta$ (polar angle), $\phi$ (azimutal angle), and velocities $\mathrm{v}^\alpha$ ($\alpha = r, \theta, \phi$), this condition translates into:

$$\mathrm{v}_0^r = 0,$$
$$r_0 = 30,\ 50,\ 80\,\mathrm{kpc}, \tag{3}$$

where the null subscript denotes an initial value. These apocentric distances are inside the present host virial radius so they are different from the true apocentres at infall. We interpret them as effective values compatible with the energy and angular momentum of the corresponding orbit (Wetzel 2011).

For simplicity, we set all the initial velocity vectors to be parallel to the $z = 0$ plane, so that

$$\mathrm{v}_0^\theta = 0. \tag{4}$$

[1]We define this parameter as the ratio between the specific angular momentum of the orbit under consideration and that of a circular orbit (which is solution of a spherical NFW potential with the same virial mass and concentration of the halo studied here) with the same specific energy.



Downloaded from https://academic.oup.com/mnras/article-abstract/492/3/4398/5675643 by University of Durham user on 25 March 2020

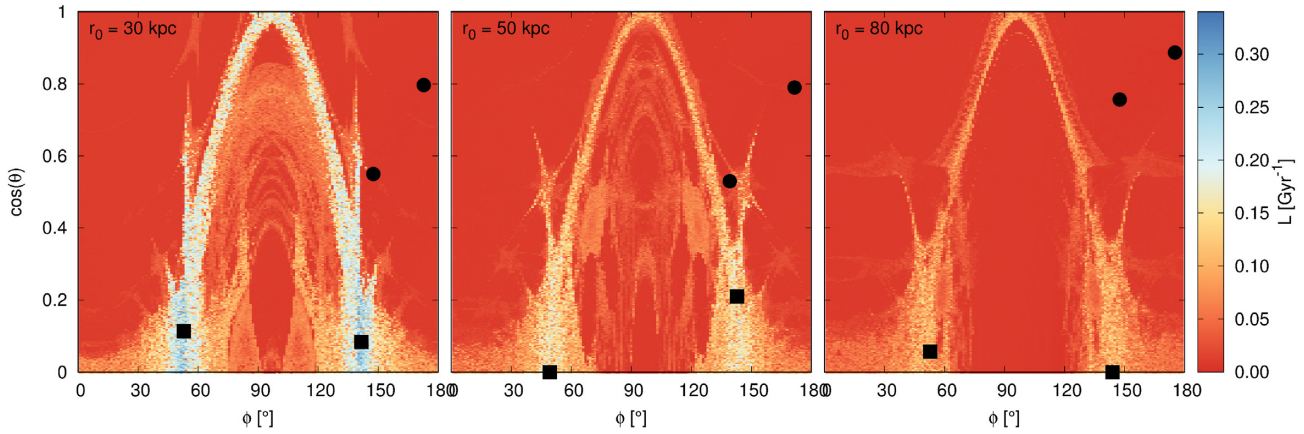


**Figure 1.** Chaoticity and selection of initial conditions for the satellites in configuration space. Each panel corresponds to a different value of the galactocentric distance $r_0$. The background colours correspond to the Lyapunov exponent, $L$, used to classify the orbits as regular (red) or chaotic (orange, blue, and white). Each black point corresponds to the initial position of the centre of mass of a progenitor (circles and squares for regular and chaotic orbits respectively). In all the cases, the initial velocity of the centre of mass of the satellites is a horizontal vector pointing to the right.

**Table 1.** Initial conditions for the centre of mass of the progenitors, radius of the equivalent circular orbit, largest Lyapunov characteristic exponent, classification and Lyapunov time (only for the chaotic ones), minimum pericentric distance, mean pericentric distance, and its standard deviation.

| Number of sat | $r_0$ (kpc) | $\phi_0$ (°) | $\cos\theta_0$ | $v_0^\phi$ (km s$^{-1}$) | $r_c$ (kpc) | $L$ (Gyr$^{-1}$) | Classification | $T_L$ (Gyr) | $r_{min}$ | $\langle r_p \rangle$ | $\sigma_p$ |
|---|---|---|---|---|---|---|---|---|---|---|---|
| 1 | 30 | 52.8 | 0.113 | 67.46 | 19.87 | 0.3344 | Chaotic | 2.99 | 2.13 | 9.31 | 3.12 |
| 2 | 30 | 141.6 | 0.083 | 67.46 | 19.87 | 0.3229 | Chaotic | 3.12 | 1.97 | 9.04 | 3.29 |
| 3 | 30 | 172.8 | 0.797 | 67.46 | 19.87 | 0.0053 | Regular | – | 7.06 | 11.25 | 1.86 |
| 4 | 30 | 147.6 | 0.550 | 67.46 | 19.87 | 0.0060 | Regular | – | 5.62 | 9.91 | 2.09 |
| 5 | 50 | 49.2 | 0.000 | 70.06 | 32.50 | 0.2380 | Chaotic | 4.16 | 4.61 | 12.37 | 5.37 |
| 6 | 50 | 142.8 | 0.210 | 70.06 | 32.50 | 0.2271 | Chaotic | 4.42 | 4.58 | 12.79 | 3.43 |
| 7 | 50 | 139.2 | 0.530 | 70.06 | 32.50 | 0.0047 | Regular | – | 5.74 | 13.07 | 3.50 |
| 8 | 50 | 171.6 | 0.790 | 70.06 | 32.50 | 0.0054 | Regular | – | 12.14 | 16.33 | 1.86 |
| 9 | 80 | 52.8 | 0.057 | 69.57 | 51.05 | 0.1766 | Chaotic | 5.72 | 7.80 | 17.79 | 6.17 |
| 10 | 80 | 144.0 | 0.000 | 69.57 | 51.05 | 0.1711 | Chaotic | 5.85 | 3.54 | 12.83 | 7.34 |
| 11 | 80 | 147.6 | 0.757 | 69.57 | 51.05 | 0.0041 | Regular | – | 16.48 | 20.29 | 3.36 |
| 12 | 80 | 175.2 | 0.887 | 69.57 | 51.05 | 0.0044 | Regular | – | 18.644 | 21.25 | 2.50 |

Finally, considering the definition of circularity $\eta$ and equations (3) and (4), we arrive to an equation for the equivalent circular radius $r_c$ together with an expression for the initial (azimutal) velocity:

$$0 = \frac{1}{2}\left[1 - \frac{r_c^2}{r_0^2}\eta^2\right]\frac{f(r_c/r_s)}{r_c} - \frac{\ln(1+r_c/r_s)}{r_c} + \frac{\ln(1+r_0/r_s)}{r_0},$$
$$v_0^\phi = \eta\frac{\sqrt{G r_c M_{200}}}{r_0}\sqrt{\frac{f(r_c/r_s)}{f(c)}}. \quad (5)$$

We have thus obtained three surfaces of initial conditions with each one being a sphere in configuration space with radius equal to $r_0$ and parametrized by the two angular variables, $\theta_0$ and $\phi_0$.

Now it is possible to study the phase-space structure of these surfaces through a classical chaos indicator. Fig. 1 shows colour coded the largest Lyapunov characteristic exponent $L$ at finite time (Benettin et al. 1980; Skokos 2010) in the plane ($\phi_0$, $\cos\theta_0$). The higher the value of this indicator, the more chaotic the orbit is. These orbits and their associated variational equations (necessary to calculate $L$) were integrated for 1000 Gyr with the eight order symplectic integrator presented in Schlier & Seiter (2000). The time-step chosen for the integrations was $\Delta t = 0.1$ Myr. We repeated the analysis using the smaller alignment index (Skokos et al. 2003, 2004), which is an alternative way of measuring the chaoticity of a system. Results obtained with both estimators are consistent. Chaotic orbits amount to 49 per cent, 44 per cent, and 32 per cent, respectively for each panel. For each apocentric distance, we selected two of the most chaotic orbits and two of the least chaotic (i.e. most regular) orbits. Table 1 shows the values of these initial conditions for the centres of the satellites. The table also shows the radius of the equivalent circular orbits, the value of the Lyapunov exponent and the classification that we infer from it. Only for the chaotic cases we include the Lyapunov time $T_L$, which is an estimation of the time it takes for two infinitely close orbits to diverge from each other by a factor $e$. In other words, it is inversely proportional to the degree of chaos of the orbit. Besides, we give the value of the smallest pericentric distance $r_{min}$, the mean pericentric distance $\langle r_p \rangle$, and the corresponding standard deviation.

### 2.3 Structure of the progenitors

The initial conditions for the $N = 10^6$ dark matter particles of the satellite were drawn from a Plummer distribution (Plummer 1911),



Downloaded from https://academic.oup.com/mnras/article-abstract/492/3/4398/5675643 by University of Durham user on 25 March 2020

whose mass inside a given radius $r$ is given by:

$$M_{\rm DM}(r) = \frac{M_{\rm DM}}{\left[1+(b_{\rm DM}/r)^2\right]^{3/2}}.$$

We assumed the following values for the total mass $M_{\rm DM}$ and the length-scale $b_{\rm DM}$:

$$M_{\rm DM} = 1.6\times10^8\,{\rm M}_\odot,$$
$$b_{\rm DM} = 0.62\,{\rm kpc},$$

which are consistent with the Sculptor galaxy and were fixed by taking into account constraints on the dark matter mass at two different radii provided by Wolf et al. (2010) and Breddels et al. (2013):

$$M_{\rm DM}(r_{1/2}=0.375\,{\rm kpc}) = 2.25\times10^7\,{\rm M}_\odot,$$
$$M_{\rm DM}(1\,{\rm kpc}) = 10^8\,{\rm M}_\odot,$$

where $r_{1/2}$ is the half-light radius.

Although the evolution of the barionic component is not considered in the $N$-body simulations, the stellar matter can be tracked through an association with the most tightly bound material in the dark matter halo. Specifically, each dark matter particle is labelled with a given value of stellar mass applying the method of Bullock & Johnston (2005), as follows. We assume that the stellar component is initially distributed as an isotropic Plummer sphere of mass $M_\star$ and length scale $b_\star$ and that it does not contribute to the gravitational potential. In this way, denoting the Plummer density and potential as $\rho_\star(r)$ and $\Phi_{\rm DM}(r)$, the stellar-to-dark mass ratio of a particle of relative specific energy $\epsilon = -(\Phi_{\rm DM}(r)+\mathbf{v}\cdot\mathbf{v}/2)$ is given by

$$\Upsilon(\epsilon) = f_\star(\epsilon)/f_{\rm DM}(\epsilon),$$

where

$$f_{\rm DM}(\epsilon) = \frac{24\sqrt{2}b_{\rm DM}^2}{7\pi^3G^5M_{\rm DM}^4}\epsilon^{7/2},$$
$$f_\star(\epsilon) = \frac{1}{\sqrt{8}\pi^2}\int_0^\epsilon \frac{{\rm d}^2\rho}{{\rm d}\Psi^2}\frac{{\rm d}\Psi}{\sqrt{\epsilon-\Psi}},$$

are respectively the dark matter and stellar phase-space distribution densities (rewritten as functions of $\epsilon$), with $\rho \equiv \rho_\star(r(\Psi))$, $\Psi \equiv \Psi_{\rm DM} = -\Phi_{\rm DM}$ and

$$\rho_\star(r) = \frac{3M_\star}{4\pi b_\star^3}\frac{1}{\left[1+(r/b_\star)^2\right]^{5/2}}.$$

Gilmore et al. (2007) showed that for any Plummer sphere that models matter in which mass follows light, the observed 2D projected half-light radius, $r_{\rm 2D}$, is exactly the scale parameter $b_\star$. Moreover, according to Sanderson, Helmi & Hogg (2015) or table B1 of Wolf et al. (2010), the 3D and 2D Plummer's half-light radii are related to each other by

$$r_{1/2} = (2^{2/3}-1)^{-1/2}r_{\rm 2D}$$

so that

$$b_\star = r_{\rm 2D} = (2^{2/3}-1)^{1/2}r_{1/2} \approx 0.766\times0.375 \sim 0.29\,{\rm kpc},$$

which is close to the value used by Breddels et al. (2013). Regarding the stellar mass, we adopted $M_\star = 10^6\,{\rm M}_\odot$ as in Breddels et al. (2013).

### 2.4 *N*-body parameters

The softening for the $N$-body simulations was chosen by performing the following three-step procedure. First of all, we applied the method used in Villalobos & Helmi (2008), obtaining a theoretical optimal softening parameter of $\tau \sim 16$ pc for our situation of $N = 10^6$ dark matter particles. Afterwards, we checked that our realization of the Plummer sphere, satisfies the scalar virial theorem, obtaining $2T/|V| = 1.00311$ for $\tau = 16$ pc and $2T/|V| = 0.99986$ for $\tau = 0$ pc, where $T$ and $V$ are respectively the kinetic energy and the virial[2] of the system. At last, we verified numerically the stability during a Hubble time of our isolated progenitor. We set the maximum time step to be $\Delta t_{\rm max} = 1$ Myr and, following the standard criterion of GADGET-2 (appendix A2 of Villalobos & Helmi 2008), we obtained an effective time step of $\Delta t_{\rm eff} = 0.4$ Myr during the whole integration.

## 3 ANALYSIS

The aim of our analysis is to determine how the presence of chaos affects our ability to detect tidal streams using data from surveys such as Gaia (de Bruijne 2012; Banik et al. 2018) or the future Large Synoptic Survey Telescope (LSST Science Collaboration et al. 2009). In order to do that, we need to specify both stream membership (i.e. whether stars in our simulations belong to the progenitor or form part of a stream) and a detectability criterion.

### 3.1 Characterization of streams: membership and detectability

For each simulated satellite, we will define its associated stream in terms of the relative distance between the stellar particles and the centre of mass of the satellite in configuration space. The centre of the satellite at time $t$ is defined as the instantaneous centre of mass of the five particles that, at the beginning of the simulation, are the most bounded. According to the definitions given in the previous section, the degree of boundedness of each particle at the beginning of the simulation is computed using the Plummer potential. At every time $t$, we define the stream as the set of particles that for any previous time $t' < t$ departed from the centre of the satellite in more than 5 kpc. The progenitor at time $t$ is defined as the complement of the stream; that is, as the set of particles that have always (for all $t' < t$) been inside a sphere of radius 5 kpc. We selected this value because it is large enough in order to include all the initial stellar mass of the progenitor and small enough in order to follow stellar streams as soon as they are formed.

Next we define a detectability criterion based on configuration space data. From an observational perspective, we would observe the stellar mass distribution in configuration space of the total stellar halo, $\rho_{\rm total}$, and would compare it with a model of the background stellar halo distribution, $\rho_{\rm halo}$, trying to identify significant overdensities. We classify a stream particle as detectable if

$$d \equiv \frac{\Delta\rho}{nE(\Delta\rho)} > 1, \tag{6}$$

[2]The virial for a gravitational system of $N$ particles with softening $\tau$ is equal to

$$V = -G\sum_{i=1}^{N-1}\sum_{j=i+1}^{N}\frac{m_im_j}{(r_{\rm ij}^2+\tau^2)^{1/2}} + \tau^2G\sum_{i=1}^{N-1}\sum_{j=i+1}^{N}\frac{m_im_j}{(r_{\rm ij}^2+\tau^2)^{3/2}}$$

where $r_{\rm ij} \equiv |\boldsymbol{r}_{\rm i}-\boldsymbol{r}_{\rm j}|$, and $\boldsymbol{r}_{\rm i}$ and $m_{\rm i}$ are respectively the position and mass of the $i$th particle. Note that for a null softening, the virial is equal to the potential energy.

Downloaded from https://academic.oup.com/mnras/article-abstract/492/3/4398/5675643 by University of Durham user on 25 March 2020

where

$$\Delta\rho = \rho_{\rm total} - \rho_{\rm halo} \tag{7}$$

is the halo overdensity (i.e. stream density), $E(\Delta\rho)$ is an estimation of the error in the determination of $\Delta\rho$ and $n$ is the statistical significance of the detection. These formulae are equivalent to saying that a stellar particle is detectable whenever the signal-to-noise ratio of the overdensity is larger than the desired detection significance.

The overdensity was estimated from the $N$-body simulations on a grid of size $h$ with a triangular shaped cloud scheme (Hockney & Eastwood 1988). The selection mechanism of $h$ will be explained ahead in this section. According to equations (6) and (7), in order to calculate $E(\Delta\rho)$, we need to take into account separate contributions from the estimations of the density of both the background stellar halo of the MW and the total stellar halo (which includes the stream particles):

$$E(\Delta\rho) = \left[E^2(\rho_{\rm total}) + E^2(\rho_{\rm halo})\right]^{1/2}. \tag{8}$$

To estimate the component $E^2(\rho_{\rm halo})$ associated to the stellar halo, we model the halo density with a power-law distribution:

$$\rho_{\rm halo}(r) = \frac{A}{(r/{\rm R}_\odot)^u}, \tag{9}$$

where $A$ and $u$ are free parameters and $\rm R_\odot$ is the Sun's galactocentric distance, for which we take a standard mean value $\rm R_\odot = 8\,kpc$. We assume that the two free parameters in this definition are independent of the velocity and adopt mean values from Hernitschek et al. (2017): $(A, u) = (10^5\,{\rm M_\odot kpc^{-3}}, 3.5)$, which were obtained from the distribution (renormalized) of RR Lyrae. The associated variance can then be computed taking into account standard error propagation:

$$\begin{aligned} E^2(\rho_{\rm halo}) = &\left[\frac{\partial\rho_{\rm halo}}{\partial A}\right]^2 E^2(A) + \left[\frac{\partial\rho_{\rm halo}}{\partial u}\right]^2 E^2(u) \\ &+ \left[\frac{\partial\rho_{\rm halo}}{\partial {\rm R}_\odot}\right]^2 E^2({\rm R}_\odot) = \rho_{\rm halo}^2 \left[\frac{E^2(A)}{A^2}\right. \\ &\left. + \ln^2(r/{\rm R}_\odot)E^2(u) + \frac{u^2}{{\rm R}_\odot^2}E^2({\rm R}_\odot)\right], \end{aligned} \tag{10}$$

where $E(A)$, $E(u)$, and $E(\rm R_\odot)$ are the standard deviations of the fitted model parameters. We will present our main results assuming hypothetical 1 per cent errors and will analyse the impact of larger errors in Section 4.3. According to equation (10), 1 per cent errors in the parameters correspond to a total error in the density of 0.5–2.5 per cent, for distances between 10 and 80 kpc, respectively.

In order to model the error $E(\rho_{\rm total})$ that corresponds to the observed density, we consider Poissonian noise, while approximating the mass $m_\star$ of every star to be equal to one solar mass. As the number of stars in a given cubic cell of volume $h^3$ is

$$N(\boldsymbol{r}) = \frac{h^3}{m_\star}\rho_{\rm total}(\boldsymbol{r}), \tag{11}$$

and its shot noise is $E(N) = \sqrt{N}$, we have that the squared shot noise of the total density is

$$E^2(\rho_{\rm total}) = \left[\frac{m_\star}{h^3}E(N)\right]^2 = \frac{m_\star}{h^3}\rho_{\rm total}. \tag{12}$$

The total density in this equation corresponds to the observed density. Since we are not working with a full mock halo catalogue, we estimated the total halo density with the addition of both the theoretical density of the stellar halo of the MW and the density of the mock stream:

$$\rho_{\rm total} = \rho_{\rm halo} + \Delta\rho. \tag{13}$$

Once we obtained all the necessary components of the error and densities on the grid, we calculated the detectability criterion defined in equation (6) on the grid and interpolated back to the particles of the simulation afterwards with the same TSC scheme employed for the density estimation. Note that a similar criterion was applied to SDSS–Gaia Catalogue data by Myeong et al. (2018) in the velocity space.

For the significance parameter, we chose a value $n = 4$, which implies a confidence in the detection of more than 99.99 per cent. The only parameter that remains to be fixed is the grid spacing $h$. While the error associated to the halo is independent of $h$, the stream density and the shot noise component of the error do depend on it (both of them grow when increasing the resolution). This implies that either the shot noise dominates (for small $h$ values) or the overdensity is very small (for large $h$). So the detectability parameter decreases towards very high or very low resolutions. In order to quantify these effects, we performed a convergence test whose result is summarized in Fig. 2. The points correspond to the time average of the fraction of stars that are detectable as a function of the spatial resolution as obtained from the simulations numbers 1 to 10. The values decrease towards very high or very low resolutions, having their maximum at $h \sim 1$ kpc, which is the value we use for the rest of our analysis.

The detectability criterion we have defined corresponds to an idealized observation. Some of the characteristics of a true detection that are not considered by our model are: the use of local background volumes, use of generalized spaces with dimension higher than three, binning determined by the uncertainties of the observed quantities, samples restricted to luminous evolved stars and mass function dependence.

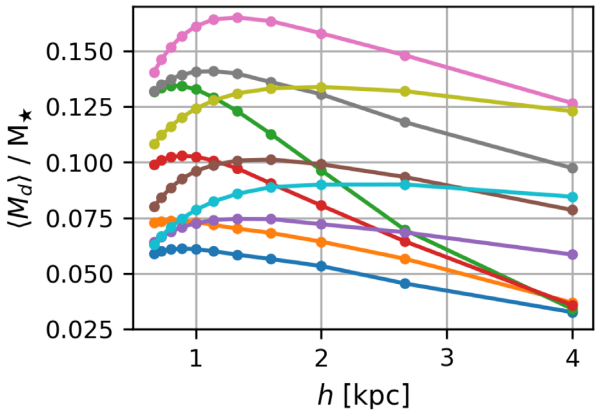


**Figure 2.** Convergence test of the detectability criterion. Left: dependence of the time average of the fraction of detectable stream mass, $\langle M_{\rm d}\rangle$, with respect to the initial stellar mass of the satellite, $M_\star$, as a function of the resolution, for satellites numbers 1–10.

## 4 RESULTS

We now summarize the results that we obtained from our simulations on the evolution of the streams an the impact of chaos on our ability to detect them.



Downloaded from https://academic.oup.com/mnras/article-abstract/492/3/4398/5675643 by University of Durham user on 25 March 2020

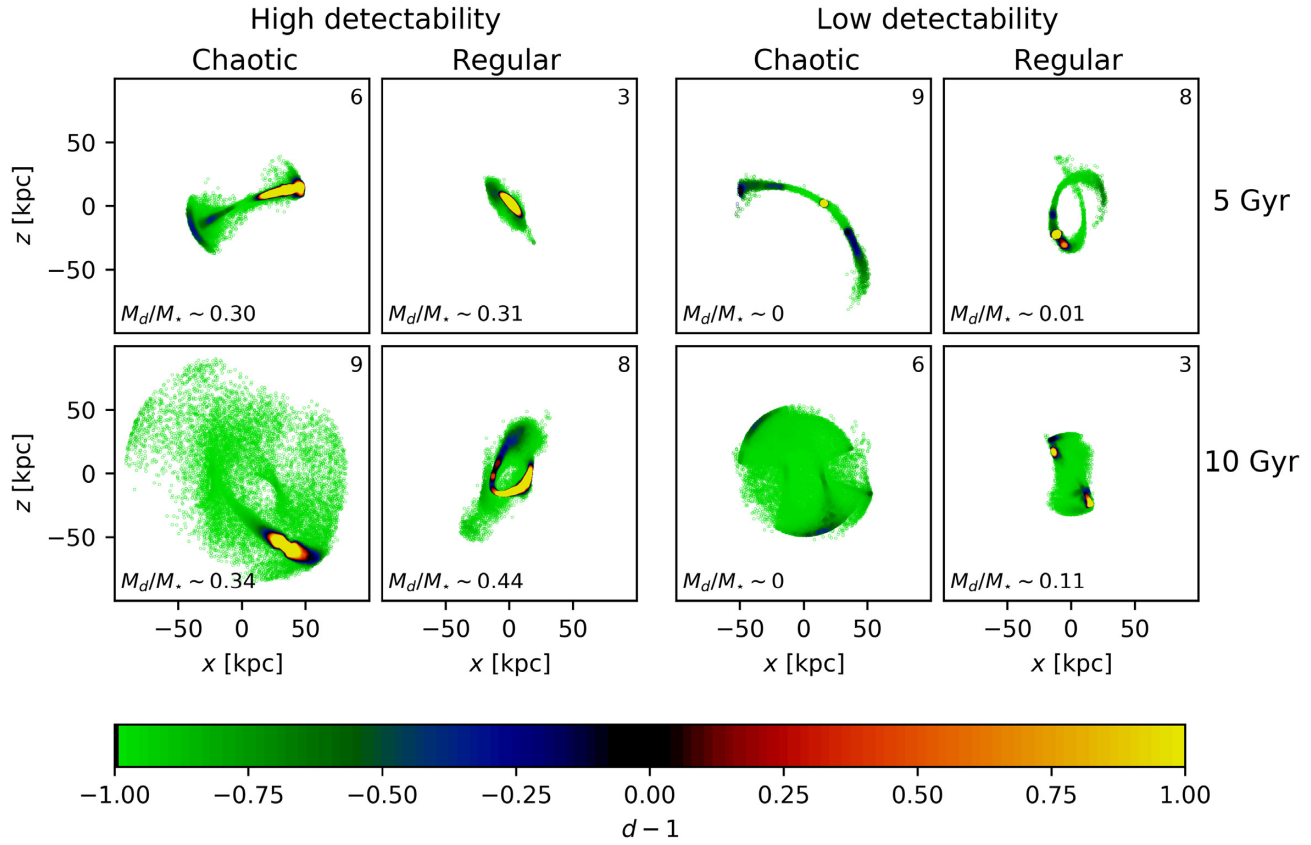


**Figure 3.** Examples of streams at times 5 Gyr (top) and 10 Gyr (bottom) with high (left) and low (right) detectable stream mass $M_{\rm d}$. The projection shown is the ($x$, $z$), colour coded with $d-1$. According to equation (6), the detectable stars are coloured red or yellow, while the undetectable stars are coloured blue or green. The satellite number is given in the top right corner of each panel, and $M_{\rm d}$ is given at the bottom of each panel. Note that among the yellow particles, the ones that belong to the progenitor do not contribute to $M_{\rm d}$. We also classify the orbits of the progenitors as regular or chaotic.

### 4.1 Visual appearance of the simulated streams

Fig. 3 shows examples of four specific streams (from satellites numbers 3, 6, 8, and 9) at 5 and 10 Gyr, projected in the plane ($x$, $z$) and colour coded according to $d-1$. Our algorithm classifies yellow and red particles as detectable, and blue and green ones as non-detectable. The black colour stands for the threshold situation. In order to sample the particles in agreement with their stellar content, we have classified the particles into five stellar mass ranges in $M_\odot$ units: 0.4–1.5, 1.5–5, 5–10, 10–50, 50–120, and plotted them using one every 20, 10, 5, 2, and 1 particles, respectively. We have not plotted particles with less than 0.4 $M_\odot$. The top labels characterize whether the stream as a whole has high or low detectability, according to its total detectable stream stellar mass $M_{\rm d}$, which is written at the bottom of each panel. It is worth noticing that satellites numbers 8 and 9 at 5 Gyr have most of their detectable stars concentrated in their respective progenitors so that these stars do not contribute to $M_{\rm d}$ at all.

A priori, one would expect that the stars that escape from a progenitor whose trajectory is in a chaotic region of phase space will quickly diffuse and not form a detectable stream. However, we find very well-defined streams in both chaotic and regular cases. In fact, we can see that there are snapshots of chaotic and regular streams that look like similar to each other, with regards to the detectability distribution in the sky. This suggests that, if there is any effect of chaos on the detectability, it must be subtle.

### 4.2 Three stages in the life of the streams

In order to better understand the results shown in Fig. 3 we analysed integrated quantities as a function of time. The panels in Fig. 4 show the outcome of such analysis for each satellite separately. The identification numbers shown in the upper left corner of each panel correspond to the same IDs shown in Table 1. The orange and green curves are the total dark matter and stellar masses of the stream, while the blue curves are the stellar mass of the stream that can be detected by our algorithm (i.e. $M_{\rm d}$). All the curves are normalized with the corresponding initial mass of the progenitor ($M_\star$ or $M_{\rm DM}$). The strong oscillations that we find in the blue curves can be analysed considering that when the particles detach from the progenitor due to the host tidal force, their dynamics becomes approximately that of an ensemble of test particles in the halo of the host galaxy. Thus, when a portion of stream is approaching its pericentre, it is expanded in coordinate space and when approaching its apocentre it is compressed. Therefore, the stream density, and consequently its detectability, present oscillations whose period correspond to the radial orbital period of the satellite. As we are not interested in this phenomenon, but on the overall properties of the detectability of the streams, we filtered these oscillations in Fourier space using the following empirical kernel:

$$W(\nu, c, s) = w(\nu, c, s)w(\nu, -c, s),$$
$$w(\nu, c, s) = 1 - \frac{1}{1 + [(\nu - c)/s]^{10}}, \quad (14)$$

Downloaded from https://academic.oup.com/mnras/article-abstract/492/3/4398/5675643 by University of Durham user on 25 March 2020

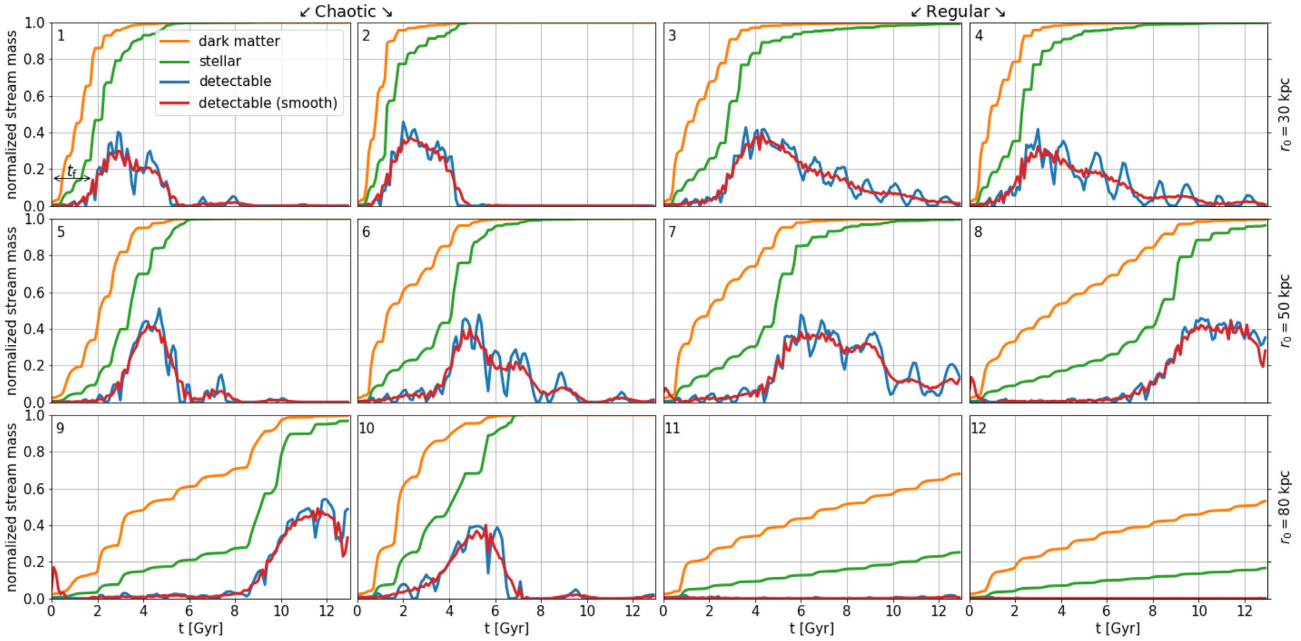


**Figure 4.** Temporal evolution of stream masses: total dark matter (orange), total stellar (green), detectable (blue), and filtered detectable (red), all of them normalized by the initial mass of the progenitor ($M_{\rm DM}$ or $M_\star$). The satellite number is placed in the top left corner of each panel. The two columns to the left and the two to the right correspond to chaotic and regular orbits of the progenitors respectively. Each row corresponds to different apocentric radii of the initial conditions (smaller apocentres above).

where $\nu$ is the coordinate in Fourier space (i.e. frequency) and we assume $(c, s) = (1.5, 1)$ Gyr$^{-1}$. These values enable us to reduce the effects associated to the radial orbital frequency of the satellites and at the same time, maintain the main features of the detectability curves. The resulting curves are shown in red in Fig. 4.

Except for satellites numbers 11 and 12, whose orbits are too far away from the host galaxy to form detectable streams, all the curves have similar qualitative behaviour. It is possible to identify three distinct phases in the evolution of the detectable part of the stream:

(i) *Quiet formation:* since the streams are formed by material that comes from the instantaneous outer layers of the progenitor and the stellar component is more concentrated than the dark matter one, most of the mass loss in the early phase belongs to the dark matter component of the satellites. The release of stars is slow and thus, the stellar streams are not detectable.

(ii) *Violent formation:* when about 80 per cent of the total dark matter mass of the progenitor is lost, the remaining core still contains the 60 per cent of the initial stellar stellar mass of the progenitor ($M_\star$). So at this point, the mass of the detectable portion of the stream increases abruptly up to a fixed value. This process is further enhanced by the fact that the potential well decreases while the particles are tidally removed from the progenitor.

(iii) *Diffusion:*[3] once the progenitor is completely destroyed, the flow of mass into the stream ceases. Diffusion in phase space dominates, reducing the density of the stream, with a consequent decline of the detectability curves. Most of the stellar stream mass becomes undetectable by the end of this last stage.

Thus, the detectable mass of a stream depends on both the rate of expulsion of stars from the satellite and the diffusion rate. The larger the former and the smaller the latter during a given time interval, the more detectable mass we will have in the stream at the end of that interval. It should be noticed that all the streams reach a detectability peak between 30 per cent and 40 per cent of $M_\star$. A consequence of this is that only a lower bound of the satellite's original stellar mass can be obtained when counting stream stars in surveys.

It would be interesting to asses how the scheme of three stages here presented is modified when the halo of the progenitor is cuspy instead of cored (Errani, Penarrubia & Tormen 2015).

### 4.3 Impact of chaos in the life of the streams

While the behaviour described above is the same for almost all the satellites, details of the transitions between different regimes depend on the orbital properties of the satellites (including their chaoticity). For instance, the red curves in Fig. 4 show that the jump in detectable mass occurs at earlier times for satellites with smaller apocentric distances. We quantify this by estimating the formation time of the streams $t_{\rm f}$ as the first instant in which the filtered detectability curves (red curves in Fig. 4) reach half of their historical maxima. Fig. 5 shows the dependence of this quantity with the smallest pericentric distance $r_{\rm s}$ that the satellite reached earlier than $t_{\rm f}$.[4] For this simulation suite, in which the initial internal structure of

[3]We use the term *diffusion* to mean a process of spreading out or divergence of deterministic orbits with nearby initial conditions. Similar approaches have been used in the study of chaotic diffusion in Hamiltonian systems by Guzzo, Efthymiopoulos & Paez (2019), Cincotta et al. (2014), Cordeiro (2006), and Cordeiro & Mendes de Souza (2005).

[4]Note that although $r_{\rm min}$ (defined in Table 1) and $r_{\rm s}$ are similar quantities, they differ in two aspects: (i) the former is computed using the symplectic orbit that corresponds to the initial condition for the progenitor while the latter is computed using the definition of the centre of mass of the



Downloaded from https://academic.oup.com/mnras/article-abstract/492/3/4398/5675643 by University of Durham user on 25 March 2020

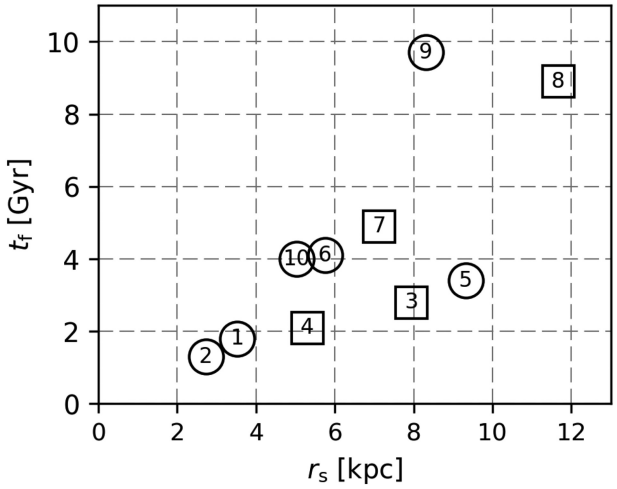


**Figure 5.** Formation time, $t_f$, of stellar streams as a function of the smallest pericentric distance, $r_s$, that takes place before $t_f$. Each point in this figure corresponds to a different satellite, identified with a label. Chaotic and regular satellites are marked respectively with circles and squares. Since satellites numbers 11 and 12 do not form detectable streams, we exclude them from the plot.

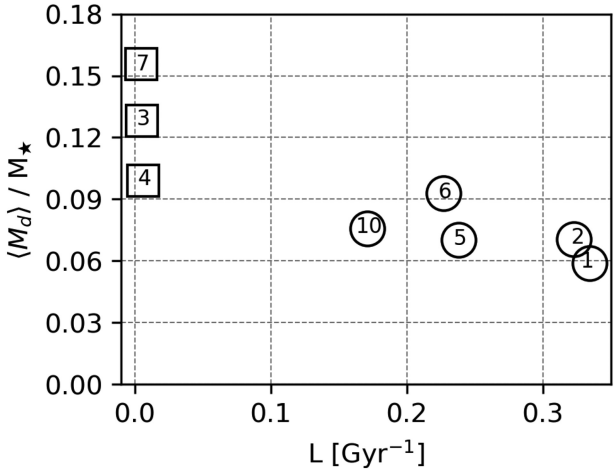


**Figure 6.** Average detectability of stellar streams, $\langle M_d \rangle$, as a function of the Lyapunov exponent $L$. Each point in this figure corresponds to a different satellite, identified with a label. Chaotic and regular satellites are marked respectively with circles and squares. The satellites numbers 8 and 9 were not included in this figure because their formation time is so late that the regime of diffusion is not well developed.

the progenitors is the same, the dominant effect that decides when the streams are formed is the typical pericentric distance of the orbits. Progenitors in orbits with smaller pericentres feel stronger tidal forces, so that their associated Roche lobes shrink faster, favouring the release of stars. Consequently, orbits with smaller pericentres tend to form detectable streams faster than orbits with greater pericentres. In Appendix A, we prove with high significance the existence of a weak correlation between $L$ and $r_{\rm min}$ for a large sample of test orbits, which in combination with the $r_s$–$t_f$ correlation implies the existence of a weak $L$–$t_f$ correlation (progenitors in chaotic orbits tend to disrupt faster than those in regular orbits).

Now we will study whether chaos has got any measurable contribution to the process of reduction of the stream observability. The speed with which the detectability of the stream decreases after its historical maximum should depend on how fast the diffusion occurs in phase space. Since the stars that leave the progenitor behave essentially as test particles in the MW halo, their posterior evolution depends on the properties of the galactic potential, which determines the diffusion rate. Regions of the phase space in which the orbits are regular or chaotic will be associated to diffusion with power-law or exponential temporal dependencies respectively (Kandrup 1998). It is expected that streams that are originated in satellites that move in chaotic orbits will be more affected by this process and will reduce more rapidly the amount of detectable mass. This will in turn also decrease the mean time interval in which the streams can be detected. We confirm this reasoning by plotting the time average of the detectable mass $\langle M_d \rangle$ against the Lyapunov exponent $L$ of the trajectory of the progenitor (see Fig. 6). The trend is that the larger the value of $L$ (i.e. the larger the degree of chaos in the surroundings of the progenitor), the smaller $\langle M_d \rangle$, and so, the smaller the probability of detecting the stream. In order to have a quantitative estimate of the effect of chaos on the detectability, we have also computed the average of $\langle M_d \rangle$ over both the regular and the chaotic streams, finding values of 0.13 and 0.07, respectively. Thus, the presence of chaos reduces the amount of average detectable mass in a 50 per cent approximately.

In order to explore the correlation when increasing the value of the errors assumed for the parameters of the stellar halo distribution ($A$, $u$, and R$_\odot$), we computed $\langle M_d \rangle$ for a cubic grid of errors between 1 and 5 per cent and found that $\langle M_d \rangle$ decreases when increasing any of these three parameter errors. Table 2 shows the Pearson correlation coefficient $\mathcal{C}_x$, between $L$ and $\langle M_d \rangle$, as a function of the relative error. We also provide the level of significance $\mathcal{L}_s$, defined as the probability of rejecting the zero hypothesis (i.e. $\mathcal{C}_x = 0$) when it is true. Inspecting at this table, it can be stated that for $\delta = 1$ per cent we can reject the zero correlation hypothesis with a certainty better than 99 per cent, while for $\delta = 2$ per cent this can be done at most with a certainty of 97 per cent. When increasing the value of $\delta$, the significance of the correlation drops below 95 per cent which is our adopted threshold value. For this reason, the test cannot certify the existence of the correlation for values of the errors larger than 2 per cent. Much significance could be gained by increasing the number of simulated streams. Summing up, if the model of the stellar halo density in configuration space is known with a precision $\leq 2$ per cent, then the probability of detecting a stellar stream is larger for regular orbits than for chaotic ones.

### 4.4 Parallel results using the velocity space

MW surveys provide information not only in configuration space, but also in velocity space. Thus, it may be worth asking whether our findings persist when performing the analysis in velocity space. We have performed a parallel detectability analysis using velocity distributions as in Myeong et al. (2018). This time the halo density is modelled with a Gaussian distribution:

$$\rho_{\rm halo}(v) = B \exp\left[-v^2/(2\sigma^2)\right]. \quad (15)$$

Throughout the analysis, we assumed that the two free parameters in this definition are independent of the position in configuration space and adopting the values $B = 10^9/(2\pi\sigma^2)^{1.5}\,{\rm M}_\odot({\rm km\,s^{-1}})^{-3}$ and $\sigma = 150$ km s$^{-1}$, which is consistent with De Lucia & Helmi (2008) and with Myeong et al. (2018), respectively.

progenitor given in Section 3.1; and (ii) the former considers a Hubble time of integration while the latter considers only times up $t_f$.

Downloaded from https://academic.oup.com/mnras/article-abstract/492/3/4398/5675643 by University of Durham user on 25 March 2020

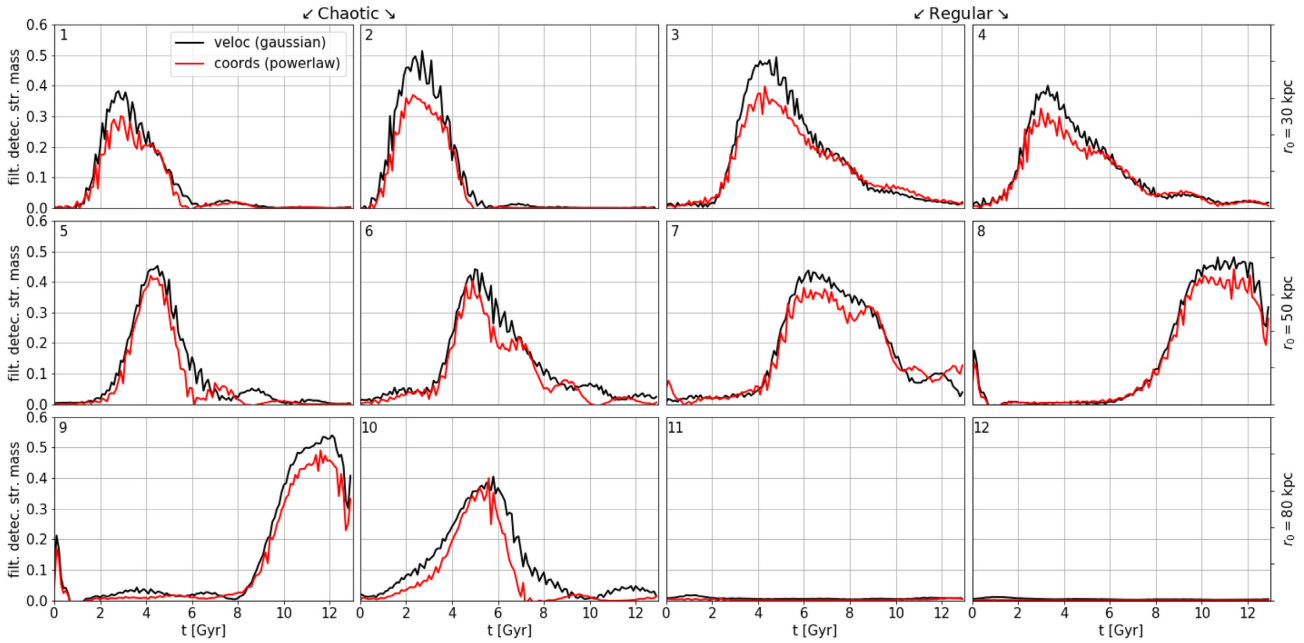


**Figure 7.** Temporal evolution of filtered detectable stream mass using coordinate (red) and velocity (black) spaces, normalized with $M_\star$. The satellite number is placed in the top left corner of each panel. The two columns to the left and the two to the right correspond to chaotic and regular orbits of the progenitors respectively. Each row corresponds to different apocentric radii of the initial conditions (smaller apocentres above).

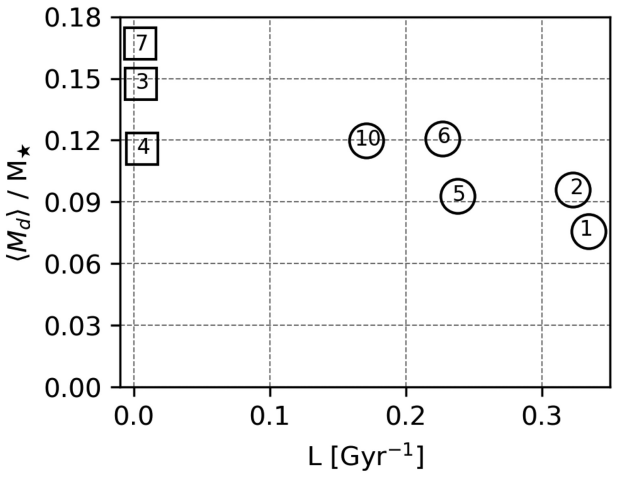


**Figure 8.** Same as Fig. 6, but using a detectability criterion in velocity space.

Fig. 7 shows the time evolution of the filtered detectable mass of the coordinate approach (in red as in fig. 4) and the velocity approach (in black). We see that both behaviours are pointwise similar so that the three stages in the life of a stream presented in Section 4.2 are recovered. Nevertheless, there is a slight variation in the maximum detectability peak attained, that in this case is about 40–50 per cent $M_\star$.

When comparing Figs 6 and 8, it can be noticed that the results on both spaces are closely similar. The coefficient $\mathcal{C}_\mathrm{v}$ in Table 2 was computed analogously to $\mathcal{C}_\mathrm{x}$ but in velocity space. The results are compatible with those presented in Section 4.3, where the significance is better than 95 per cent as long as $\delta \leq 1$ per cent. This is another example of the robustness of the detectability criterion presented in this work.

**Table 2.** Correlation coefficients, $\mathcal{C}_\mathrm{x}$ and $\mathcal{C}_\mathrm{v}$, between $L$ and $\langle M_\mathrm{d} \rangle$ as a function of the relative error using$\delta = E(A)/A = E(u)/u = E(\mathrm{R}_\odot)/\mathrm{R}_\odot = E(B)/B = E(\sigma)/\sigma$. The significance $\mathcal{L}_s$ is provided between braces.

| $\delta$ (per cent) | $\mathcal{C}_\mathrm{x}$ $\{\mathcal{L}_\mathrm{s}\}$ | $\mathcal{C}_\mathrm{v}$ $\{\mathcal{L}_\mathrm{s}\}$ |
|---|---|---|
| 1 | −0.85 {0.5} | −0.84 {0.6} |
| 2 | −0.73 { 3} | −0.61 {10} |
| 3 | −0.62 { 9} | −0.37 {36} |
| 4 | −0.54 {15} | −0.24 {56} |
| 5 | −0.48 {22} | −0.09 {85} |

## 5 CONCLUSIONS

The objective of this paper is to study theoretically the influence of chaos on the detectability of Galactic stellar streams. For this purpose, we analysed a suite of 12 simulations of minor mergers. In all of them the host galaxy was modelled with a triaxial generalization of the NFW profile and the satellites were modelled with a Plummer sphere with parameters that resemble the Sculptor galaxy. The only difference between these experiments was the initial condition of the centre of mass of the progenitor. Half of these initial conditions were chosen to give birth to chaotic orbits while the rest were chosen so that their corresponding orbits were regular. The chaoticity had previously been determined by computing the largest Lyapunov characteristic exponent $L$ of each orbit.

Each satellite was embedded in the host halo potential and was evolved with a self-gravitating $N$-body code (GADGET-2). These tidal stream simulations were analysed with a detectability criterion that depends on the stream stellar density and on a smooth model of the density of the stellar halo. This criterion works independently with either configuration or velocity data, giving similar outcomes.

We found that the evolution of the detectability (detectable mass $M_\mathrm{d}$) of the stellar stream goes through three distinct stages: quiet formation, violent formation, and diffusion. During the initial phase the satellite looses most of the outer layers of its dark halo, but just



Downloaded from https://academic.oup.com/mnras/article-abstract/492/3/4398/5675643 by University of Durham user on 25 March 2020

a small proportion of its total stellar mass. The rate of stellar stream formation is low until the progenitor has lost about 80 per cent of its dark matter halo when this rate abruptly increases, setting in the beginning of the violent formation stage. All the stellar streams reach now a detectability peak of magnitude between 30 and 40 per cent of the original stellar mass of the satellite for the detectability criterion applied in configuration space. For the criterion in velocity space, this quantity ranges between 40 and 50 per cent. These upper bounds imply that counting stream stars leads to a considerable underestimation of the initial mass of the progenitor.

Hamiltonian diffusion, which is always present and tends to wash out the stream structures, becomes dominant when the stellar injection stops due to the total disruption of the progenitor. This event settles the diffusion stage that is characterized by a decay of $M_{\rm d}$. The fact that $M_{\rm d}$ decays faster for a stream whose progenitor behaves chaotically than for those associated to regular orbits, is captured in the existence of a correlation between the Lyapunov exponent $L$ and the temporal average of the detectability $\langle M_{\rm d} \rangle$.

Through a significance analysis of the correlation, it was found that the previous result is valid as long as the errors in the stellar halo model parameters are smaller than about 1 per cent. In other words, with our criterion and model errors of 1 per cent, chaos reduces the detectability. Consequently, if a host galaxy has a significant proportion of chaotic orbits and if we are working with a model and star count data highly precise (e.g. $\lesssim 1$ per cent), the probability of detecting streams will be proportionally lower.

As the satellite destruction time is correlated with the chaoticity through its dependence on pericentric distances, the proportion of chaotic orbits should have also incidence in statistical studies of the number of dSph satellites. For example, ensembles of progenitors in chaotic trajectories will tend to disrupt and form streams faster than progenitors in regular ones.

## ACKNOWLEDGEMENTS

CLL acknowledges support from STFC consolidated grant ST/L00075X/1 and ST/P000541/1 and ERC grant ERC-StG-716532-PUNCA. MM and DDC acknowledge support from CONICET (PIP0436), UNLP (G127), and the program Erasmus Mundus EURICA. CLL thanks Shaun Cole for discussions. MM thanks Amina Helmi, Shoko Jin, Tjitske Starkenburg and Nicolás Maffione for discussions. We thank the referee for the constructive comments.

## REFERENCES

Amorisco N. C., 2015, MNRAS, 450, 575
Banik N., Bertone G., Bovy J., Bozorgnia N., 2018, J. Cosmol. Astropart. Phys., 2018, 061
Beaugé C., Ferraz-Mello S., Michtchenko T. A., 2012, Res. Astron. Astrophys., 12, 1044
Benettin G., Galgani L., Giorgilli A., Strelcyn J.-M., 1980, Meccanica, 15, 9
Bonaca A., et al., 2019, preprint (arXiv:1910.00592)
Bovy J., 2016, Phys. Rev. Lett., 116, 121301
Breddels M. A., Helmi A., van den Bosch R. C. E., van de Ven G., Battaglia G., 2013, MNRAS, 433, 3173
Bullock J. S., Johnston K. V., 2005, ApJ, 635, 931
Burkert A., Silk J., 1999, in Klapdor-Kleingrothaus H. V., Baudis L., eds, Dark Matter in Astrophysics and Particle Physics, Springer-Verlag, Berlin, p. 375
Carpintero D. D., Muzzio J. C., Navone H. D., 2014, MNRAS, 438, 2871
Cincotta P. M., Efthymiopoulos C., Giordano C. M., Mestre M. F., 2014, Phys. D Nonlinear Phenom., 266, 49
Conselice C. J., Yang C., Bluck A. F. L., 2009, MNRAS, 394, 1956
Contopoulos G., 2002, Order and Chaos in Dynamical Astronomy, Springer-Verlag, Berlin
Contopoulos G., Harsoula M., 2012, Celest. Mech. Dyn. Astron., 113, 81
Cordeiro R. R., 2006, AJ, 132, 2114
Cordeiro R. R., Mendes de Souza L. A., 2005, A&A, 439, 375
Davies R. D., Wright A. E., 1977, MNRAS, 180, 71
de Bruijne J. H. J., 2012, Ap&SS, 341, 31
De Lucia G., Helmi A., 2008, MNRAS, 391, 14
Debattista V. P., Roškar R., Valluri M., Quinn T., Moore B., Wadsley J., 2013, MNRAS, 434, 2971
Deg N., Widrow L., 2013, MNRAS, 428, 912
Deg N., Widrow L., 2014, MNRAS, 439, 2678
Dehnen W., 2000, AJ, 119, 800
Dehnen W., McLaughlin D. E., Sachania J., 2006, MNRAS, 369, 1688
Efthymiopoulos C., Voglis N., Kalapotharakos C., 2007, in Benest D., Froeschle C., Lega E., eds, Lecture Notes in Physics, Special Features of Galactic Dynamics, Springer-Verlag, Berlin, p. 297
Errani R., Penarrubia J., Tormen G., 2015, MNRAS, 449, L46
Fardal M. A., Huang S., Weinberg M. D., 2015, MNRAS, 452, 301
Fux R., 2001, A&A, 373, 511
Gilmore G., Wilkinson M. I., Wyse R. F. G., Kleyna J. T., Koch A., Evans N. W., Grebel E. K., 2007, ApJ, 663, 948
Guzzo M., Efthymiopoulos C., Paez R. I., 2019, JNS, Springer US, p. 94
Hayashi E., Navarro J. F., Springel V., 2007, MNRAS, 377, 50
Helmi A., White S. D. M., 1999, MNRAS, 307, 495
Helmi A., White S. D. M., de Zeeuw P. T., Zhao H., 1999, Nature, 402, 53
Helmi A., Veljanoski J., Breddels M. A., Tian H., Sales L. V., 2017, A&A, 598, A58
Hendel D., Johnston K. V., 2015, MNRAS, 454, 2472
Hernitschek N. et al., 2017, ApJ, 850, 96
Hockney R. W., Eastwood J. W., 1988, Computer Simulation using Particles, Taylor & Francis, Inc., USA
Hunter C., 2005, Ann. New York Acad. Sci., 1045, 120
Johnston K. V., Law D. R., Majewski S. R., 2005, ApJ, 619, 800
Kandrup H. E., 1998, MNRAS, 301, 960
Karademir G. S., Remus R.-S., Burkert A., Dolag K., Hoffmann T. L., Moster B. P., Steinwandel U. P., Zhang J., 2019, MNRAS, 487, 318
Kauffmann G., White S. D. M., 1993, MNRAS, 261, 921
Law D. R., Majewski S. R., 2010, ApJ, 714, 229
Łokas E. L., Mamon G. A., 2001, MNRAS, 321, 155
LSST Science Collaboration, 2009, preprint (arXiv:0912.0201)
Lux H., Read J. I., Lake G., Johnston K. V., 2013, MNRAS, 436, 2386
Maffione N. P., Gómez F. A., Cincotta P. M., Giordano C. M., Cooper A. P., O'Shea B. W., 2015, MNRAS, 453, 2830
Maffione N. P. et al., 2018, MNRAS, 478, 4052
Malhan K., Ibata R. A., Martin N. F., 2018, MNRAS, 481, 3442
Mantha K. B. et al., 2018, MNRAS, 475, 1549
Martí J. G., Giuppone C. A., Beaugé C., 2013, MNRAS, 433, 928
Martínez-Delgado D., Peñarrubia J., Gabany R. J., Trujillo I., Majewski S. R., Pohlen M., 2008, ApJ, 689, 184
Merritt D., Valluri M., 1996, ApJ, 471, 82
Morales G., Martínez-Delgado D., Grebel E. K., Cooper A. P., Javanmardi B., Miskolczi A., 2018, A&A, 614, A143
Morbidelli A., 2010, Comp. Rend. Phys., 11, 651
Myeong G. C., Evans N. W., Belokurov V., Amorisco N. C., Koposov S. E., 2018, MNRAS, 475, 1537
Navarro J. F., Frenk C. S., White S. D. M., 1997, ApJ, 490, 493
Pearson S., Küpper A. H. W., Johnston K. V., Price-Whelan A. M., 2015, ApJ, 799, 28
Pearson S., Starkenburg T. K., Johnston K. V., Williams B. F., Ibata R. A., Khan R., 2019, ApJ, 883, 87
Plummer H. C., 1911, MNRAS, 71, 460
Price-Whelan A. M., Johnston K. V., Valluri M., Pearson S., Küpper A. H. W., Hogg D. W., 2016a, MNRAS, 455, 1079
Price-Whelan A. M., Sesar B., Johnston K. V., Rix H.-W., 2016b, ApJ, 824, 104

Downloaded from https://academic.oup.com/mnras/article-abstract/492/3/4398/5675643 by University of Durham user on 25 March 2020

Sanderson R. E., Helmi A., Hogg D. W., 2015, ApJ, 801, 98
Schlier C., Seiter A., 2000, Comput. Phys. Commun., 130, 176
Sesar B. et al., 2015, ApJ, 816, L4
Shipp N. et al., 2018, ApJ, 862, 114
Siopis C., Kandrup H. E., 2000, MNRAS, 319, 43
Skokos C., 2010, in Souchay J., Dvorak R., eds, Lecture Notes in Physics, Vol. 790. Springer Verlag, Berlin, p. 63
Skokos C., Antonopoulos C., Bountis T. C., Vrahatis M. N., 2003, Prog. Theor. Phys. Suppl., 150, 439
Skokos C., Antonopoulos C., Bountis T. C., Vrahatis M. N., 2004, J. Phys. A Math. Gen., 37, 6269
Springel V., 2005, MNRAS, 364, 1105
Tsiganis K., Varvoglis H., Dvorak R., 2005, Celest. Mech. Dyn. Astron., 92, 71
Vallejo J. C., Sanjuan M. A. F., 2016, A&A, 595, A68
Valluri M., Merritt D., 1998, ApJ, 506, 686
Vera-Ciro C., Helmi A., 2013, ApJ, 773, L4
Villalobos Á., Helmi A., 2008, MNRAS, 391, 1806
Vogelsberger M., White S. D. M., Helmi A., Springel V., 2008, MNRAS, 385, 236
Voglis N., Tsoutsis P., Efthymiopoulos C., 2006, MNRAS, 373, 280
Watkins L. L., Evans N. W., An J. H., 2010, MNRAS, 406, 264
Wetzel A. R., 2011, MNRAS, 412, 49
Wolf J., Martinez G. D., Bullock J. S., Kaplinghat M., Geha M., Muñoz R. R., Simon J. D., Avedo F. F., 2010, MNRAS, 406, 1220
Wright A. E., 1972, MNRAS, 157, 309
Zhu Q., Hernquist L., Marinacci F., Springel V., Li Y., 2017, MNRAS, 466, 3876

## APPENDIX A: CORRELATION BETWEEN CHAOS AND PERICENTRIC DISTANCE

For 19 810 test particle orbits that densely sample the orbits whose initial conditions are displayed in the middle panel of Fig. 1 (i.e. for $r_{\rm apo} = 50$ kpc), we have plotted their values of the largest Lyapunov exponent at finite time $L$ versus their smallest pericentric distances attained during a Hubble time $r_{\rm min}$, in the central panel of Fig. A1. We also show the corresponding marginal distributions with blue histograms, noticing a peaked clump of regular orbits for $\log(L) \lesssim -4.55$ ($L \lesssim 0.01$). The right-hand side border of this clump can be used to divide the $\log(L) - r_{\rm min}$ plane approximately into chaotic and regular orbits, with the aid of a green line. Considering only the chaotic orbits, we have made the corresponding marginal histograms in orange colour, from which it can be deduced that chaotic orbits have a larger probability of reaching smaller pericentric distances than regular ones.

In order to give further support to this result, we have classified the points into four sets according to the threshold values of $\log(L) = -4.55$ and $r_{\rm min} = 7$ kpc (horizontal red line). We counted the number of points in each set (clockwise and starting from the top left set): 8949, 2959, 5380, and 2522, respectively. Moreover, we have computed the correlation coefficient between $L$ and $r_{\rm min}$, obtaining a value of $r = -0.34$. and the Student test gave a significance level of $\alpha = 0$ per cent, implying that there is certainly a non zero correlation between both quantities.

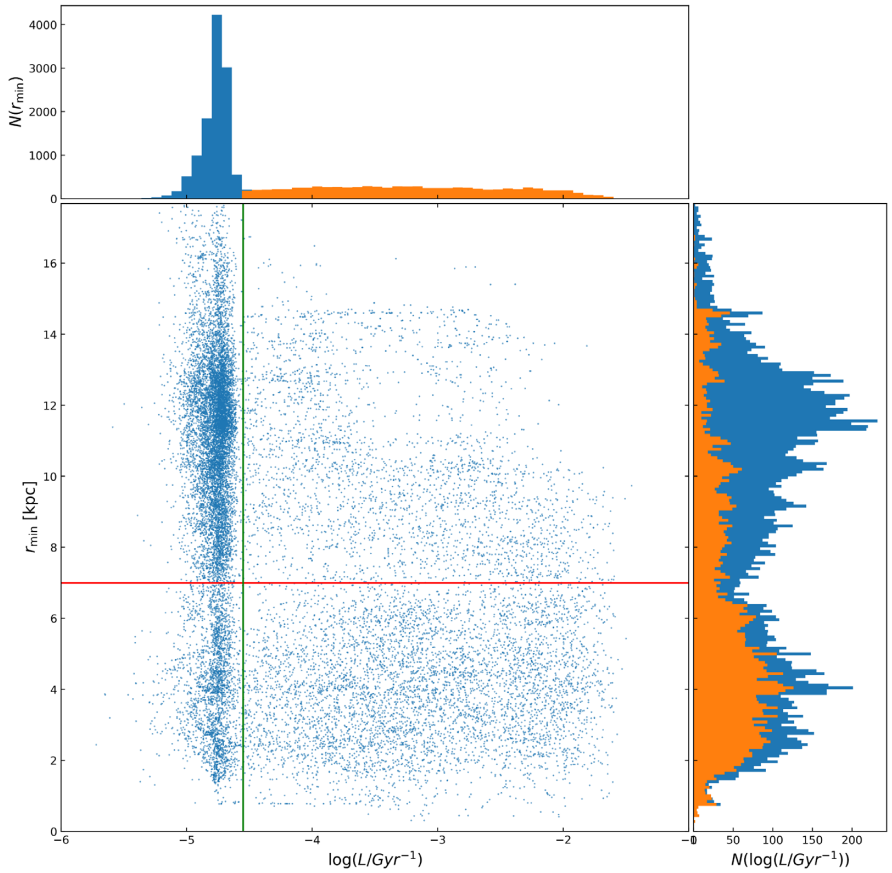


**Figure A1.** $\log(L)$ versus $r_{\rm min}$ for 19 810 test particle orbits whose initial conditions belong to the bidimensional surface with $r_{\rm apo}$ =50 kpc (middle panel of Fig. 1). Marginal histograms of $L$ and $r_{\rm min}$ are shown in blue. The orange histograms correspond to the chaotic orbits only (i.e. those at the right-hand side of the vertical line).

This paper has been typeset from a TEX/LATEX file prepared by the author.



Downloaded from https://academic.oup.com/mnras/article-abstract/492/3/4398/5675643 by University of Durham user on 25 March 2020